FULL PAPER

A Versatile Nanotheranostic Agent for Efficient Dual-Mode Imaging Guided Synergistic Chemo-Thermal Tumor Therapy

Xiaojun Cai, Xiaoqing Jia, Wei Gao, Kun Zhang, Ming Ma, Shige Wang, Yuanyi Zheng, Jianlin Shi, and Hangrong Chen**

The integration of efficient imaging for diagnosis and synergistic tumor therapy into a single-component nanoplatform is much promising for high efficacy tumor treatment but still in a great challenge. Herein, a smart and versatile nanotheranostic platform based on hollow mesoporous Prussian blue nanoparticles (HMPBs) with perfluoropentane (PFP) and doxorubicin (DOX) inside, has been designed, for the first time, to achieve the distinct in vivo synergistic chemo-thermal tumor therapy and synchronous diagnosis and monitoring by ultrasound (US)/photoacoustic (PA) dual mode imaging. The prepared HMPBs show excellent photothermal conversion properties with large molar extinction coefficient ($\approx 1.2 \times 10^{11}$ M^{-1} cm^{-1}) and extremely high photothermal conversion efficiency (41.4%). Such a novel theranostic nanoplatform is expected to overcome the inevitable tumor recurrence and metastasis resulting from the inhomogeneous ablation of single thermal therapy, which will find a promising prospect in the application of noninvasive cancer therapy.

1. Introduction

Chemotherapy is one of the most commonly used approaches for cancer treatment. However, the anticancer drugs in free formulation generally result in severe side effects on healthy tissues and the reduction of therapeutic efficacy due to its unspecific delivery. Taking account of these drawbacks, several nanomedicine strategies have been developed over past decades. Typically, liposome has been considered as drug delivery system (DDS) with excellent biocompatibility and biodegradability.[1] However, several shortcomings including poor stability, low loading drug capacity, and uncontrollable drug release, have limited its further clinical application. Compared to organic DDSs, the recently reported inorganic materials, e.g., silica and carbon with mesoporous structure, have shown substantially increased loading capacity and on-demand drug release profile.[2,3] Nevertheless, their degradation mechanisms and long-term toxicity have not been well understood to date. Thus, it is greatly desired to construct a kind of novel DDS of both excellent biocompatibility and high performances to satisfy the clinical requirements in drug delivery application.

Recently, near-infrared (NIR, λ = 700–1100 nm) laser-induced photothermal therapy has attracted much interest for tumor therapy as a minimally invasive approach.[4,5] However, it fails in eradicating tumor by photothermal therapy alone because of the inhomogeneous heat distribution within tumor tissue, thus resulting in inevitable tumor recurrence and metastasis. Previous studies have demonstrated that the efficient combination of NIR photothermal ablation and chemotherapy can significantly increase the sensitivity of chemotherapy compared to those sole treatments,[6,7] leading to the synergistic therapeutic efficacy. Generally, two major strategies of nanometer-sized DDSs have been developed to realize combination of NIR photothermal ablation and chemotherapy. The typical one is combination of metal-based nanoparticles as photothermal conversion agents (PTCAs) and drug-loaded mesoporous material/organic compounds as drug carriers, e.g., mesoporous silica-coated gold nanorods,[8] gold nanoshells on silica nanorattles,[9] gold nanorods-capped magnetic core/mesoporous silica shell nanoellipsoids,[10] DNA-coated gold nanorods,[11] and so on. Nevertheless, the complex preparation process and potential long-term toxicity hinder their further clinical application. Moreover, the exogenous coating material on PTCAs generally generates unexpected thermal resistance, lowering the photothermal conversion efficiency. The newly developed strategy is directly loading with anticancer drug into PTCAs, such as graphene[12] and transition metal sulfide,[7] mostly by chemical interaction or electrostatic adsorption. Thereinto, a kind of 3D hollow mesoporous materials, e.g., gold nanocage[13] or hollow copper sulphide,[14] has attracted much interest, since it can greatly increase drug loading capacity owing to their high specific surface area and huge cavity.[14,15] In spite of hollow mesoporous structure increasing the loading capacity of cargoes, many DDSs often suffer from the absence of enough effective binding sites between cargoes and carriers, which leads to limited loading capacity. An ideal biocompatible carrier with high enough loading capacity of drugs to raise therapeutic efficacy for tumor is in great desire for tumor therapy.

Dr. X. Cai, X. Jia, Dr. K. Zhang, Dr. M. Ma, Dr. S. Wang, Prof. J. Shi, Prof. H. Chen
State Key Laboratory of High Performance Ceramics and Superfine Microstructure
Shanghai Institute of Ceramics
Chinese Academy of Sciences
200050 Shanghai, P.R. China
E-mail: jlshi@mail.sic.ac.cn; hrchen@mail.sic.ac.cn
W. Gao, Prof. Y. Zheng
Second Affiliated Hospital of Chongqing Medical University
400016 Chongqing, P.R. China

DOI: 10.1002/adfm.201403991

The integration of imaging and therapeutic capability into a single platform has shown great potentials in drug delivery, image-guided minimally invasive therapy, and so on. However, how to achieve the synergistic therapy with synchronous imaging diagnosis and treatment monitoring for tumor by using single-component carrier is still a great challenge.[16] Ultrasound (US) imaging has been well known as a multifunctional, noninvasive, and low-cost imaging technology, which can realize real-time imaging. Nevertheless, US imaging is generally incapable of early diagnosis of tumor, owing to its limited spatial resolution and the poor contrast. Photoacoustic (PA) imaging is a newly developed technology which can break through the depth and resolution limits of optical imaging, and provides much higher spatial resolution and contrast than US imaging.[17] Therefore, the combination of US and PA dual mode imaging is hopeful to achieve the early diagnosis and the real-time therapy monitoring, as well as the assessment after treatment. Thereinto, an ideal contrast agent is highly desired for facilitating both deep tumor visualization and high contrast and spatial resolution.

It is well known that Prussian blue (PB) has been approved by USA Food and Drug Administration (FDA) as a clinical medicine for the treatment of radioactive exposure. Recently, many researchers[18,19] have focused on its photothermal therapy effect, since it shows a strong absorption in the NIR region (λ = 650–900 nm), attributing to the charge transfer transition between Fe(II) and Fe(III).[19]

Herein, a smart and versatile theranostic nanoplatform with single component based on hollow mesoporous Prussian blue nanoparticles (HMPBs) has been developed for the in vivo highly efficient synergistic chemo-thermal tumor therapy, guided by synchronous imaging diagnosis and therapy monitoring using US and PA dual-mode imaging for the first time. The loading capacity of doxorubicin (DOX) is as high as 1782.2 mg g^{-1}, owing to its distinctive hollow mesoporous structure and enough effective binding sites Fe(III). Moreover, a series of detailed in vivo biocompatibility evaluations of HMPBs, including time courses (up to 50 days) of blood and histological changes in normal tissues after intravenous injection of HMPBs, have been conducted to confirm their excellent pharmacokinetics and negligible long-term toxicity. Such a novel nanoplatform is promising to overcome the inevitable tumor recurrence and metastasis resulting from the inhomogeneous ablation of single thermal therapy, which we believe, can find a new avenue for potential application in high efficient and noninvasive cancer therapy.

2. Results and Discussions

2.1. Design and Characterization of HMPBs

With a face-centered cubic structure, PB is a mixed-valence iron hexacyanoferrate. The middle Fe(II) and Fe(III) iron, bridged by the CN– chemical groups, are carbon-bound and nitrogen-bound, respectively, and can be cleaved in the acid environment. The highly uniformly dispersed HMPBs showed an average particle diameter of about 236 nm with outershell thickness of around 43 nm (**Figure 1**a,b and Figure S1, Supporting Information), which were successfully prepared using polyvinylpyrrolidone (PVP) as a protectant, and hydrochloric acid (HCl) as an etchant. As evidenced by the apparent contrast difference in the representative high-magnification transmission electron microscopy (TEM) images (Figure 1c–e), HMPBs were obtained by the controllable etching procedure, accompanying with morphology changing from mesoporous structure to core–shell structure and eventually to the hollow mesoporous structure. In addition, the corresponding element mapping (Figure 1f–i) further confirms the successful creation of inner cavity in the HMPBs. Electron diffraction taken from one whole particle of mesoporous PBs and HMPBs confirms the single crystalline structure (the insets of Figure 1c,e), consistent of X-ray diffraction of HMPBs (Figure S2, Supporting Information), indicating that hollow mesoporous structure will not alter their crystallinity.

2.2. HMPBs as Stable Nanocarriers

Owing to hollow mesoporous structure, large specific surface area and pore volume (Figure S3, Supporting Information), HMPBs can be supposed as ideal carriers to encapsulate anticancer drug, siRNA, and/or other guest molecules. As shown in **Figure 2**a, HMPBs can be homogeneously dispersed in water, PBS, cell medium (DMEM), and fetal bovine serum, with almost the same dynamic light scattering (DLS) distribution. These solutions can keep stable even after three months for storage. Herein, DOX is chosen as a drug model and loaded into HMPBs with extremely high efficiency (loading efficiency of DOX: 98%, loading capacity of DOX: 1782.2 mg g^{-1}), as indicated by the UV–vis–NIR spectroscopy and the inset digital photos of DOX solutions before and after interaction with HMPBs (Figure 2b). The results of FTIR spectra of DOX, HMPBs, and DOX-loaded HMPBs are indicative of the successful drug loading (Figure 2c). The extraordinarily high loading capacity, which is much higher than those of the most reported carriers,[2,20] can be attributed to the distinctive characteristics of hollow mesoporous structure with huge cavity and numerous mesopores in the outershell, the presence of electrostatic interaction between HMPBs (negative-charged) (Figure S4, Supporting Information) and DOX (positive-charged), as well as strong coordinative bonding between inherent Fe(III) in the structure of HMPBs and chemical groups (e.g., amino and carbonyl) of DOX at pH 7.4. The further encapsulation of perfluoropentane (PFP) into the DOX-loaded HMPBs has little influence for the DOX loading capacity and efficiency, since it was carried out after the loading of DOX. Moreover, the DOX releasing from HMPBs exhibits a typical sustained pH and temperature-responsive release profiles (Figure 2d). It is worth noting that only a small amount of DOX (4.4% after 48 h) can be released at pH 7.4, and the linkages/bonds between DOX and carriers will be weakened at reduced pH values and increased temperatures. When reducing the pH values from 7.4 to 5.0 at 37.5 °C, the DOX release percentage increased from 4.4% to 34.7% after 48 h, and while the temperature changed from 37.5 to 42.5 °C at pH 5.0, the DOX release percentage showed further increase to 41.8% (Figure 2d), which is greatly beneficial to minimize the side effects of chemotherapeutics and enhance the antitumor efficiency.

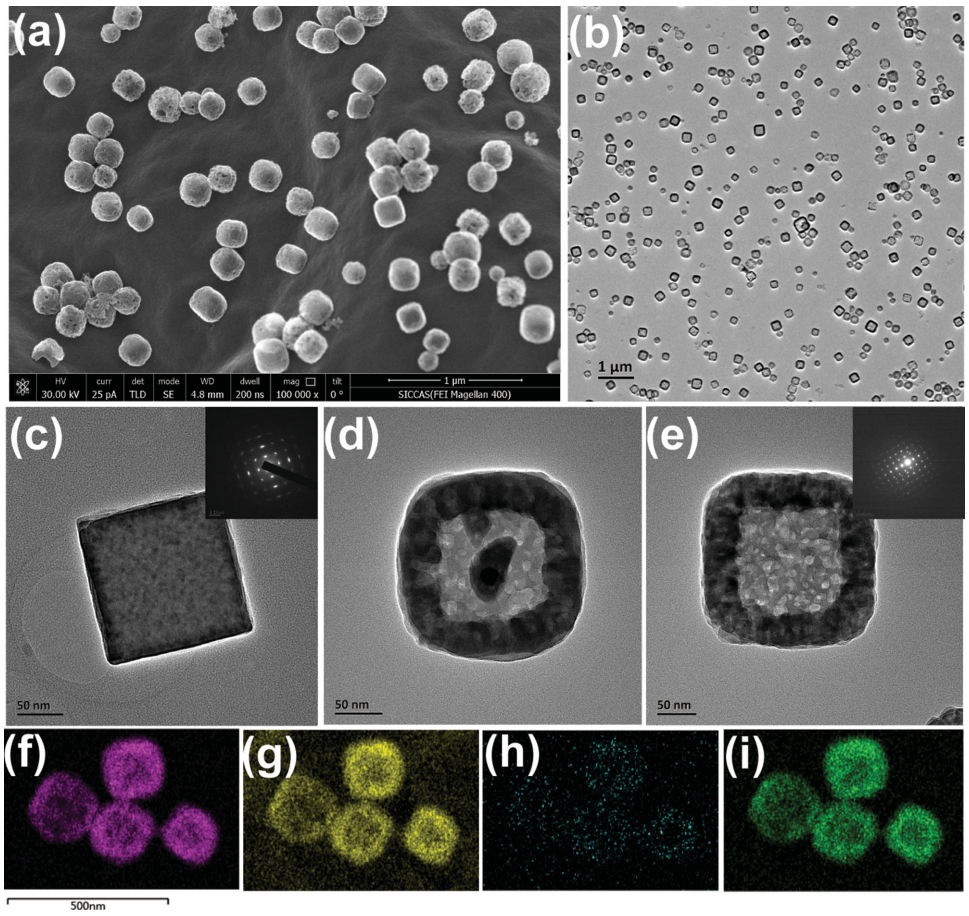

Figure 1. Characterizations of HMPBs. a) SEM imaging and b) TEM imaging of HMPBs. Typical TEM images of HMPBs after etching for varied time periods: c) 0, d) 3, e) 4 h (insets: SAED imaging of c) MPBs and d) HMPBs). The corresponding elemental mappings of HMPBs f) iron, g) carbon, h) potassium, and i) nitrogen.

2.3. The Photothermal Conversion Property of HMPBs

To explore the photothermal conversion property of HMPBs, the HMPBs aqueous solution was examined by using UV–vis–NIR spectroscopy. HMPBs exhibit a broad and strong NIR absorption band from around 600 to 900 nm (**Figure 3**a). Herein, the molar extinction coefficient ε is one of the most important parameters to determine the NIR photoabsorption capability of PTCA, which can be calculated to be $\approx 1.2 \times 10^{11}$ M^{-1} cm^{-1} at 808 nm (see the Supporting Information for the detailed calculations) for HMPBs. This value is comparable to that of Au nanostructure ($\approx 2 \times 10^{11}$ M^{-1} cm^{-1} at 800 nm),[21] and much higher than those of carbon nanotubes ($\approx 7.9 \times 10^{6}$ M^{-1} cm^{-1} at 808 nm),[22] Cu_{2-x} Se ($\approx 7.7 \times 10^{7}$ M^{-1} cm^{-1} at 970 nm),[23] and Cu_{2-x}S ($\approx 1.2 \times 10^{9}$ M^{-1} cm^{-1} at 980 nm).[24]

To further verify the potential of HMPBs as an ideal PTCA, HMPBs aqueous solution at concentrations of 0, 10, 20, 50, and 100 ppm were exposed to the 808 nm laser at a power density of 3.5 W cm^{-2} for 10 min, respectively. An obvious concentration-dependent temperature increase was observed (Figure 3b). Besides, HMPBs exhibited remarkable photostability under NIR irradiation for ten cycles (Figure 3c) and presented almost the same absorbance even under ten cycles (Figure 3d). Furthermore, the photothermal conversion efficiency η of HMPBs was calculated by a modified method similar to Korgel's report.[23] The detailed calculations of photothermal conversion efficiency could be found in Equations (S3)–(S11), Supporting Information, based on the results of time constant of heat transfer and the maximum steady-state temperature from Figure S5, Supporting Information. Therefore, the photothermal conversion efficiency of HMPBs was calculated to be 41.4%, which is significantly higher than that of Au nanorods (21%),[21] Cu_{2-x} Se (22%),[23] Cu_{2-x}S (25.7%),[24] and gold nanovesicles (37%).[25]

The high molar extinction coefficient and the high photothermal conversion efficiency indicate that HMPBs possess excellent photothermal conversion properties, thus can be used as an ideal PTCA for the potential application in anticancer treatment.

In addition, the effects of DOX and PFP on the photothermal property of HMPBs are investigated in vitro. As shown in Figure S6, Supporting Information, all the samples of HMPBs, DOX-loaded HMPBs, and DOX/PFP-loaded HMPBs with same concentration of HMPBs exhibit the same NIR absorption band from around 600 to 900 nm, either before or after laser irradiation, indicating that the loading of DOX and/or PFP in HMPBs has little effect on the photothermal property of HMPBs. Additionally, it is noting that after irradiation, the absorption intensity of both DOX-loaded HMPBs and DOX/PFP-loaded

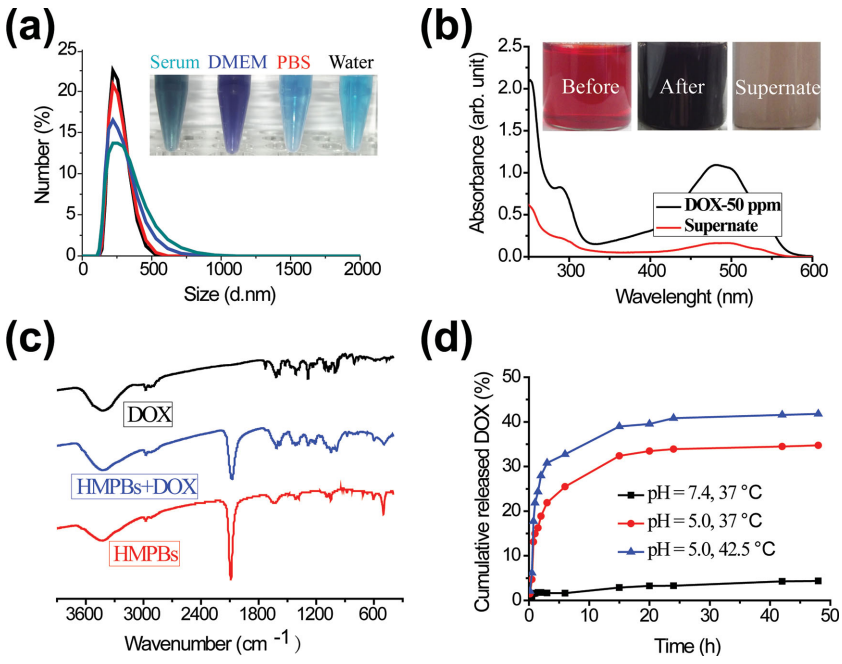

Figure 2. Drug loading and pH/temperature-responsive release. a) DLS curve of HMPBs dispersed in fetal bovine serum (FBS, green), cell mediate culture (DMEM, blue), phosphate buffer solution (PBS, red), water (black). b) UV–vis–NIR spectroscopy of DOX solutions before and after interaction with HMPBs (inset: the representative photos of DOX solution before (left) and after interaction with HMPBs (middle: before centrifugation, right: after centrifugation)). c) FTIR spectra of DOX, HMPBs, and DOX-loaded HPMBs. d) In vitro release profiles of DOX/PFP-loaded HMPBs under different pH values (pH = 7.4 and pH = 5.0) and temperatures (37 and 42.5 °C).

HMPBs has increased in the band from 400 to 530 nm, which is ascribed to the absorption of the released DOX.

2.4. In Vitro Synergistic Therapeutic Efficacy

Inspired by the outstanding photothermal conversion properties, the in vitro therapeutic efficiency of DOX/PFP-loaded HMPBs was further investigated in detail. No significant cytotoxicity of HMPBs was observed for all the three different types of cells, even at a high concentration of 3.2 mg mL^{-1} (**Figure 4**a), preliminarily indicative of good biocompatibility of HMPBs. In addition, the hemolysis test showed that the hemolysis rates of various concentrations of HMPBs are all lower than 0.5%, which is of great importance for HMPBs via intravenous injection (Figure 4b). 3-[4,5-Dimethylthiazol-2-yl]-2,5-diphenyltetrazolium bromide (MTT) assay was performed to quantitatively measure the cell viabilities after incubating Hela cancer cells with PBS, free DOX, HMPBs, and HMPBs-DOX with or without NIR irradiation. The free DOX group (24.6%) has higher toxicity than the HMPBs+DOX group (13.6%), which is due to the limited DOX release from HPMBs. The HMPBs+NIR group leads to 34.9% cell mortality rate, while the HMPBs+DOX+NIR group shows the toxicity of 51.2% cancer cells being killed (Figure 4c). Therefore, the nominal efficiency of additive therapeutic therapy ($T_{additive}$) with the combination of chemo and thermal therapy can be calculated according to Equation (1)[26]

$$T_{additive} = (1 - f_{chemo} \times f_{thermal}) \times 100\% \quad (1)$$

where f is the fraction of surviving cells after each treatment. The calculated additive value of $T_{additive}$ is 43.7%, which is higher than the single chemotherapy (13.6%) or sole photothermal therapy (34.9%), but significantly lower than the measured therapeutic efficacy of the HMPBs+DOX+NIR group (51.2%), definitely proving the distinct synergistic effect of chemo-thermal therapy in vitro (Figure 4d). Moreover, the distinct synergistic effect of chemo-thermal therapy in vitro can be seen in the other types of cancer cells (4T1 and PANC1) (Figure S7, Supporting Information).

2.5. US and PA Dual-Mode Imaging Both In Vitro and In Vivo

Since the passively accumulated amount of HMPBs (5.83% ID g^{-1}) within tumor 24 h postintravenous injection was higher than those of other time points as shown in Figure S8, Supporting Information, the investigations of in vivo photothermal therapy and US/PA imaging were conducted in 24 h after intravenous injection. Mice bearing Hela tumor were intravenously injected with DOX/PFP-loaded HMPBs (total dose = 200 µL, $C_{[DOX]}$ = 1.8 mg mL^{-1}, $C_{[HMPBs]}$ = 1.2 mg mL^{-1}) and subjected to the 808 nm laser exposure (1 W cm^{-2}, 3 min). The change of local temperature was monitored with an infrared thermal camera. It could be found that the surface temperature of tumor rapidly increased from 35.7 to 44.4 °C in 3 min, while the surrounding tissue near the tumor only showed a moderate temperature of ≈39 °C. In contrast, tumor without DOX/PFP-loaded HMPBs injection showed only 3 °C elevation within 3 min (**Figure 5**a,b).

To achieve the synergistic therapy with synchronous imaging diagnosis and treatment monitoring for tumor by using single-component carriers, PFP, a kind of hydrophobic and thermosensitive organic compound with its phase-change temperature from liquid to gas at around 29 °C, was then infused into the cavity of the DOX-loaded HMPBs by vacuuming. Obvious large number of bubbles emerged when the DOX/PFP-loaded HMPBs dispersion was heated to 42 °C, while few bubbles could be found both in DOX/PFP-loaded HMPBs dispersion and PBS at 20 °C, respectively. The gray value of DOX/PFP-loaded HMPBs solution at 42 °C is almost fourfold higher than that of DOX/PFP-loaded HMPBs solution and PBS at 20 °C (Figure 5c). The generated bubbles showed great potential to act as an enhanced ultrasound contrast agent. PA imaging was employed to evaluate the PA properties of HMPBs. It is obvious to observe a linear correlation between HMPBs concentration and the corresponding PA signal (Figure 5d). DOX/PFP-loaded HMPBs showed great potential to be both enhanced ultrasound contrast agent and PA imaging agent. 2D US and PA imaging

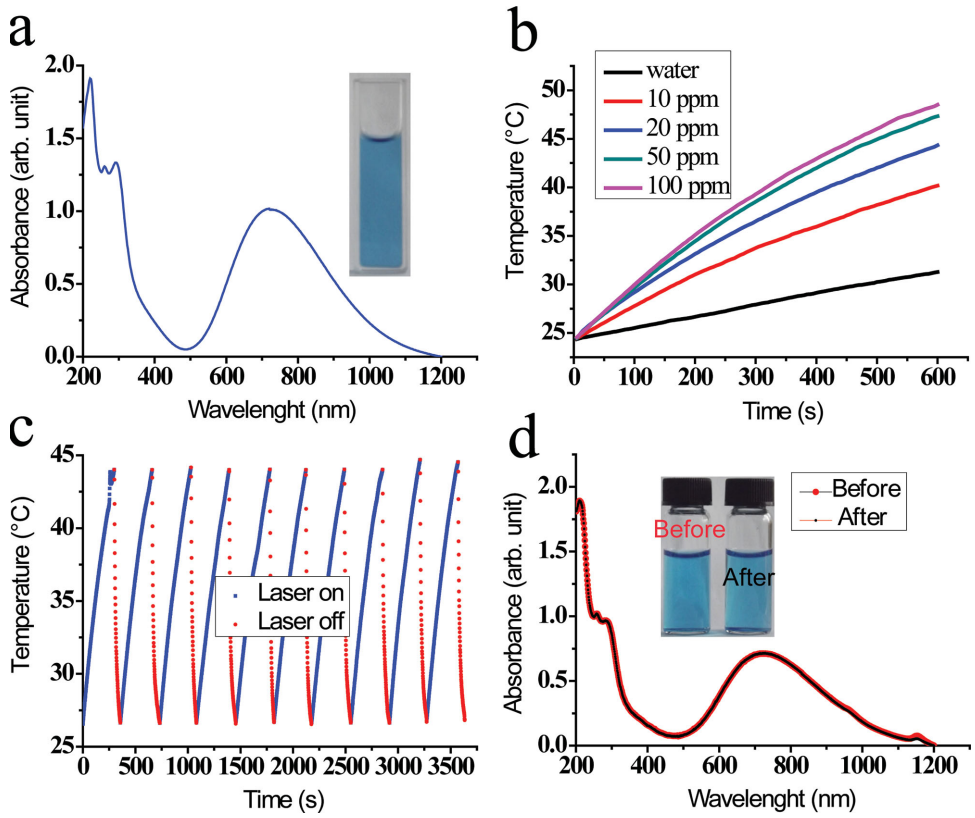

Figure 3. The photothermal conversion property of HMPBs. a) UV–vis–NIR spectroscopy of HMPBs aqueous solution (inset: the digital photo of HMPBs solution). b) Heating curves of water and HMPBs solutions of different concentrations (0, 10, 20, 50, 100 ppm) under 808 nm laser irradiation at the power density of 3.5 W cm^{-2}; c) Temperature variations of HMPBs; and d) UV–vis–NIR spectroscopy of HMPBs under the continuous irradiations of 808 nm laser for ten cycles. (Inset: the representative photos of HMPBs solution before (left) and after ten cycles (right)).

of tumor were acquired before and 24 h after the injection of DOX/PFP-loaded HMPBs. Though the standard phase-change temperature of PFP (29 °C) is lower than body temperature (37 °C), this phase-change temperature could obviously increase when DOX/PFP-loaded HMPBs were injected in the body mainly because of the additional blood pressure in vivo, which can be confirmed by the in vivo US imaging before and after injection in Figure 5e. It can be found that there is almost no variation of ultrasonic signals in the tumor region after 24 h injection of DOX/PFP-loaded HMPBs before laser exposure, demonstrating good stability of PFP in HMPBs in vivo. In addition, it is clear that the intensity of PA signal increased by 128%, from 0.39 ± 0.06 to 0.89 ± 0.09 a.u. (Figure 5e,f), after intravenous injection of DOX/PFP-loaded HMPBs, confirming the excellent photothermal performance of HMPBs. And the remarkable enhanced US signals under laser irradiation (denoted as the circle in Figure 5e), can be attributed to the generation of gas bubbling, since the temperature of the tumor increased to 44.5 °C after irradiation, which was high enough to induce the liquid–gas phase change of PFP. More interestingly, it is noting that the PA signals have received a little more increase after laser irradiation, as shown in Figure 5f, which can also be ascribed to the liquid–gas phase change of PFP with the increased temperature. Since the occurrence of inertial cavitations derived from gas bubbling would bring the local thermal effect to some extent around the tumor issues, which could be beneficial for the enhanced PA signals.

In order to further confirm both the effective accumulation of DOX/PFP-loaded HMPBs in the tumor site and the enhanced US and PA signals without the effect of endogenous substance, the tumors were dissected out after irradiation (denoted as "substract" in Figure 5e). Both the enhanced US and PA images signals were still present at the withdrawn tumor tissue, indicating that DOX/PFP-loaded HMPBs had indeed accumulated into the tumor site by enhanced permeability and retention effect, thus showing distinctive capability of thermal/US/PA imaging.

Thanks to the distinctive hollow mesoporous structure, the prepared HMPBs can be loaded with both anticancer drug (e.g., DOX) and phase-change materials (e.g., PFP). When exposed to laser, the accumulated DOX/PFP-loaded HMPBs within tumor can transform the absorbed NIR light into heat, causing PFP bubbling with the increasing temperature. Therefore, the generated bubbles could act as the ultrasound contrast agent to sensitize the US imaging signal on the one hand. On the other hand, the HMPBs show high intrinsic molar extinction coefficient at 808 nm of four orders of magnitude higher than, for example, previously reported carbon nanotube-based PA imaging agents.[22] Therefore, this novel versatile nanoplatform, consisting of single component,

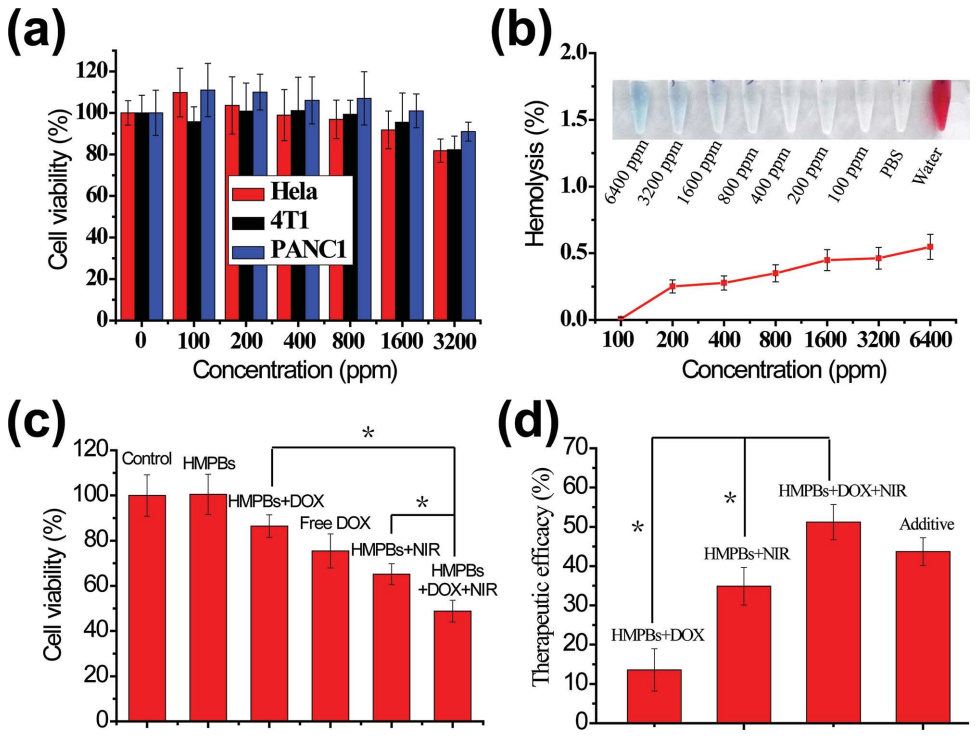

Figure 4. The in vitro synergistic therapeutic efficacy. a) Cell viability of HMPBs solution at various concentrations (0, 100, 200, 400, 800, 1600, 3200 ppm, mean ± s.e.m., $n = 6$). b) Hemolysis of HMPBs solution at various concentrations (mean ± s.e.m., $n = 3$). The mixtures were centrifuged to detect the presence of hemoglobin in the supernatant visually (inset). c) Cytotoxicity assay of Hela cells in the presence of PBS, HMPBs + DOX, free DOX without irradiation, HMPBs and HMPBs + DOX groups with laser irradiation (808 nm laser for 5 min at power density of 1 W cm^{-2}) (mean ± s.e.m., $n = 6$, $^*P < 0.05$). d) Therapeutic efficacy of chemotherapy, photothermal therapy, chemo-thermal therapy, and additive therapeutic efficacy (mean ± s.e.m., $n = 6$, $^*P < 0.05$).

possesses the capacity of high NIR absorption for PA imaging and the PFP bubbles for enhanced US imaging. More importantly, the as-injected HMPBs can be retained in the tumor tissue, which allows for repeated imaging without necessary of multiple injections.

2.6. In Vivo Synergistic Therapeutic Efficacy

Encouraged by the outstanding in vitro photothermal conversion performance, the in vivo therapeutic efficiency was further investigated in detail. Herein, the optimized 1 W cm^{-2} power density of 808 nm laser with 3 min duration was chosen for the better study on the synergistic effect between chemotherapy and photothermal therapy for tumor, since the lower laser power density with shorter treatment time is much desired in the invasive tumor therapy. First, time courses of histological changes in various tissues and blood index of mice were conducted to reveal the potential in vivo toxicity of HMPBs (Figure S9, Supporting Information), indicating that the HMPBs are promising as an ideal carrier applied in DDS since no significant toxicities in vivo can be detected. The in vivo blood half-life of drug carrier is an important indicator of metabolism and removal rate, which is of great significance in the pharmacokinetics. The in vivo blood half-life of HMPBs has been calculated to be 194 min (Figure S10, Supporting Information), which is much longer than many other drug carriers.[5,27] The long in vivo blood half-life of HMPBs can be attributed to the surface PVP modification and high dispersity of HMPBs.

Moreover, the in vivo therapeutic efficacy of HMPBs-induced chemo-thermal therapy for cancer treatment was investigated. Five groups ($n = 6$) of Hela tumor-bearing female nude mice were used. Compared to the control group with uncontrolled growth of tumor in 26 days, all the treatment groups showed inhibited tumor growth (**Figure 6**a,b). Since the DOX/PFP-loaded HMPBs were readily more internalized by cancer cells than free DOX, the HMPBs+DOX/PFP group without NIR irradiation showed a higher tumor inhibitory rate than free DOX. Much enhanced inhibitory rate could be observed for the HMPBs/PFP+NIR group, attributing to the photothermal effect of HMPBs. However, such a treatment only demonstrates an inhibitory effect on the tumor growth, but fails in regress or complete removing the tumor. In order to acquire much enhanced efficacy in tumor treatment, synergistic chemo- and photothermal tumor therapy was carried out. It could be found that the relative tumor volume had significantly decreased after being treated with DOX/PFP-loading HMPBs and laser irradiation (Figure 6b). More interestingly, the tumor completely disappeared in four weeks post-treatment, which could be visually confirmed by comparing the tumors after different treatments in various time durations, as shown in the representative digital photos (Figure 6a). In addition, the body weight of the mice in the control group and all the treatment groups did not have any noticeable changes during the treatment (Figure S11,

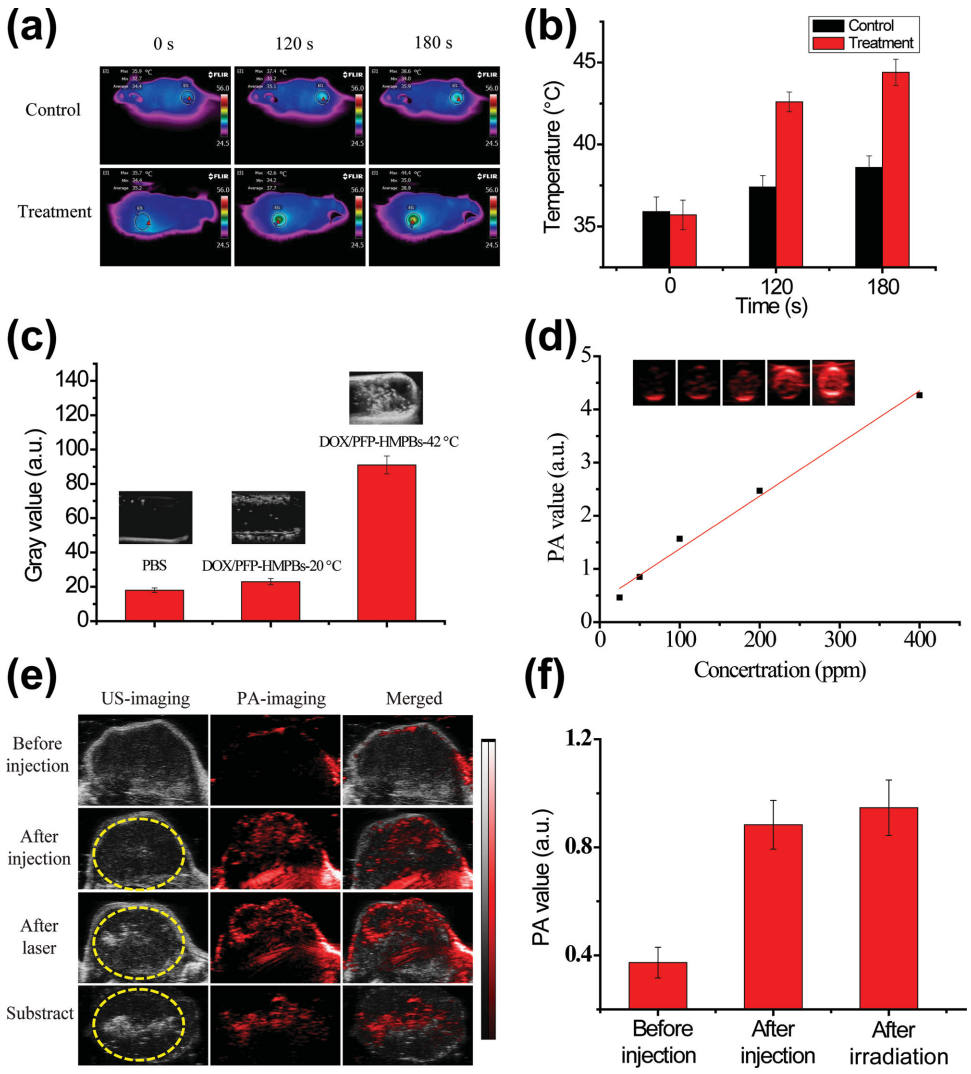

Figure 5. In vivo thermal/US/PA imaging. a) IR thermal images of control and treatment groups, and b) temperature variation of tumor-bearing mice with PBS (control) and HMPBs intravenous injections, and exposed to 808 nm laser for 3 min at the power density of 1 W cm^{-2} (mean ± s.e.m., n = 6). c) The gray value of in vitro US imaging (the inset of photos from left to right: PBS at 20 °C, DOX/PFP-loaded HMPBs solution at 20 °C, and DOX/PFP-loaded HMPBs solution at 42 °C); d) PA values of DOX/PFP-loaded HMPBs at various concentrations (the inset: PA imaging of various concentrations of DOX/PFP-loaded HMPBs solution). e) In vivo 2D US and PA imaging of tumor tissue and f) the corresponding PA values of tumor tissue before injection, after injection and after injection under laser irradiation. (mean ± s.e.m., n = 6).

Supporting Information), demonstrating satisfactory in vivo biocompatibility and biosafety of HMPBs. Furthermore, the additive inhibition efficiency of tumor was used to demonstrate the synergistic effect of chemo-thermal therapy. Herein, the additive tumor inhibition ratio of chemo-thermal therapy could be calculated by using the equation below

$$T_{\text{treatment}} = (1 - f_{\text{chemo}} \times f_{\text{thermal}}) \times 100\% \quad (2)$$

$$f_{\text{treatment}} = \frac{V_{\text{treatment}}}{V_{\text{control}}} \times 100\% \quad (3)$$

Here, f is the relative tumor growth rate after each treatment, and V is the relative tumor volume. It is clear that the measured tumor inhibition ratio of the HMPBs+DOX/PFP+NIR group is much higher than that of the other control groups, and significantly higher than those of calculated values (additive group) beyond five days (Figure 6c), confirming the in vivo chemo-thermal synergistic therapy.

Haematoxylin and eosin (H&E) staining of heart, liver, spleen, lungs, and kidney were carried out after laser irradiations for 30 days (Figure 6d). No observable changes between the healthy mice (control) and the HMPBs+DOX/PFP+NIR group can be found, indicating that HMPBs possess excellent in vivo biocompatibility. Thus, the prepared HMPBs can be potentially used as an intelligent NIR light-mediated multifunctional DDS.

3. Conclusion

In summary, an intelligent theranostic nanoplatform based on HMPBs with PFP inside, has been designed, for the first time, to

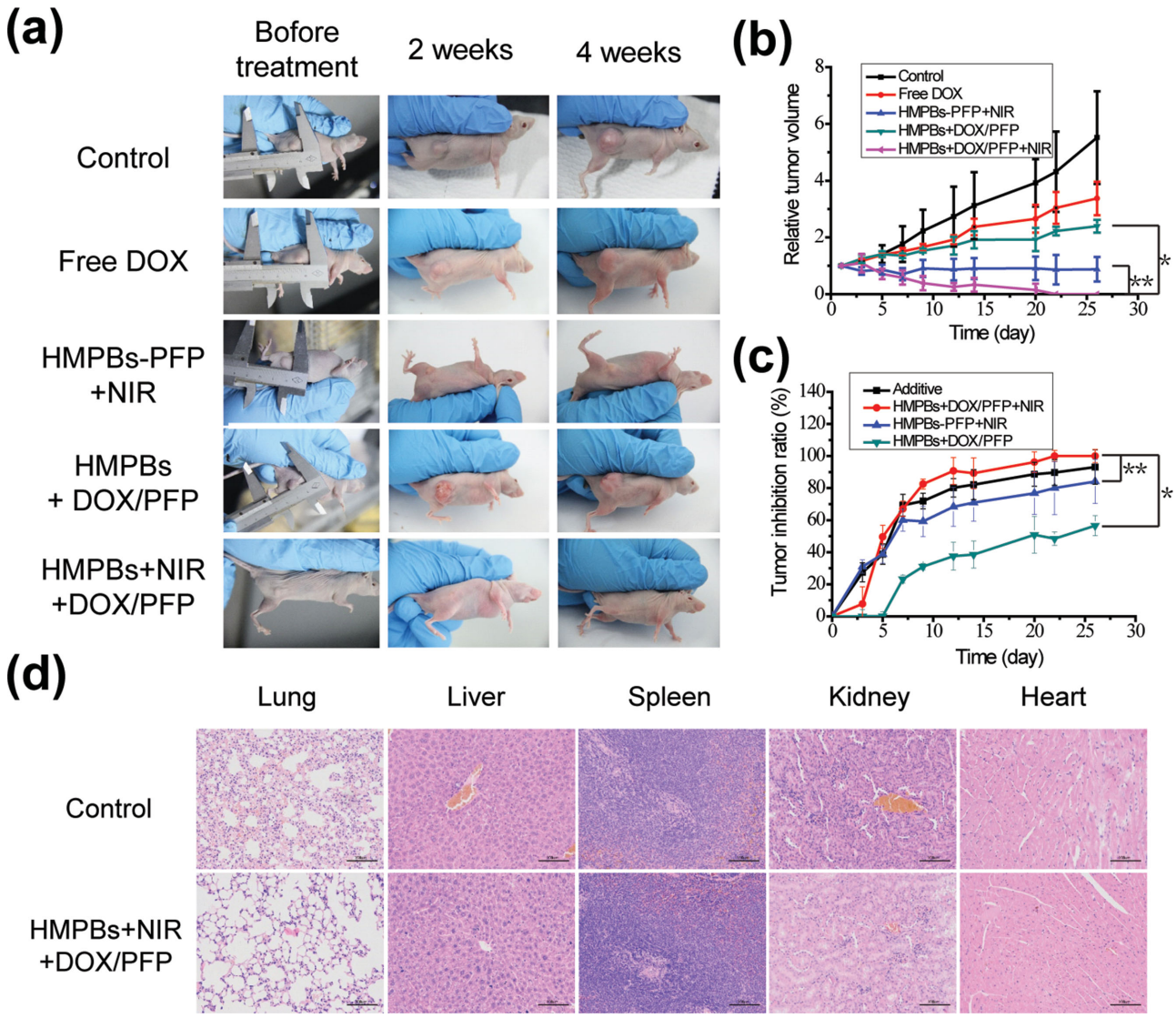

Figure 6. In vivo therapeutic efficacy of HMPBs-based therapeutic nanoplatform. a) Representative photos of mice bearing Hela tumor after different treatments for varied time periods; b) The relative tumor volumes of mice treated with PBS, free DOX, HMPBs-PFP+NIR irradiation, HMPBs+DOX/PFP, HMPBs+DOX/PFP+NIR (mean ± s.e.m., $n = 6$, $^{*}P < 0.05$,$^{**}P < 0.01$); c) Tumor inhibition ratio of the HMPBs+DOX/PFP+NIR group and additive tumor inhibition ratio of chemo-thermal therapy (mean ± s.e.m., $n = 6$, $^{*}P < 0.05$,$^{**}P < 0.01$); d) Histological changes in various tissues (lung, liver, spleen, kidney, heart) of mice after intravenous injection of PBS (control) and DOX/PFP-loaded HMPBs under irradiation.

successfully achieve the in vivo synergistic chemo-thermal tumor therapy and synchronously diagnosis and therapy monitoring by US/PA dual mode imaging. The excellent photothermal property is attributed to its high molar extinction coefficient ($\approx 1.2 \times 10^{11}$ M^{-1} cm^{-1}) and very high photothermal conversion efficiency (41.4%) of our prepared HMPBs. The achieved ultra-high drug loading capacity up to 1782 mg g^{-1} is mainly due to hollow mesoporous structure and coordination bonds between inherent Fe(III) and chemical groups (e.g., amino and carbonyl) of DOX. The as-synthesized HMPBs exhibit the distinctive characteristics of hollow mesoporous structure with huge cavity and numerous mesopores in the outershell, and the presence of electrostatic interaction between HMPBs (negative-charged) and DOX (positive-charged), as well as strong coordinative bonding between inherent Fe(III) in the structure of HMPBs and chemical groups (e.g., amino and carbonyl) of DOX at pH 7.4, which endows HMPBs with extraordinarily high loading capacity of anticancer drug DOX of 1782.2 mg g^{-1}. These linkages/bonds will be weakened at reduced pH values and/or increased temperature, thus the loaded drug can be readily released at lower pH value (e.g., tumor sites) and/or higher temperature, which is beneficial to enhance the antitumor efficiency and reduce the side effects of chemotherapy. With the extremely high loading capacity of DOX and inherent excellent photothermal conversion property, the DOX/PFP-loaded HMPBs present the distinct synergistic effect in the chemo-thermal therapy. The in vivo experiments confirmed that the measured synergistic tumor inhibition ratio is higher than that of theoretical calculating value (additive group) after five days, proving the excellent synergistic effect in the chemo-thermal therapy for tumor, which is promising

to overcome the inevitably tumor recurrence and metastasis resulted from the inhomogeneous ablation of single thermal therapy. Moreover, this single-component nanoplatform based on HMPBs can make it possible to completely eradicate cancer cells through the integration of more various therapeutic modes for tumor, such as photothermal ablation therapy, chemotherapy, radiotherapy, gene therapy, and so on, which, as we believe, can pave a new avenue for the future noninvasive cancer therapy.

4. Experimental Section

Materials: All chemicals were of analytical grade and used directly without further purification. PVP (K30), potassium ferricyanide ($K_3[Fe(CN)_6]$), HCl (36.0%–38.0%) and PFP (Sigma-Aldrich Co. LLC.) were purchased from Sinopharm chemical Reagent Co., Ltd.

Preparation of Hollow Mesoporous Prussian Blue Nanoparticles: The HMPBs were prepared according to the reported method.[28] First, PVP (3.0 g), $K_3[Fe(CN)_6]$ (132 mg), and HCl solution (0.01 M, 40 mL) were mixed under magnetic stirring. After obtaining a clear solution, the vial was put into an electric oven at 80 °C for 24 h. Then, through centrifuged and washed in distilled water several times, mesoporous Prussian blue nanoparticles (MPBs) were obtained. PVP (5 mg mL^{-1}) were added to the solution of MPBs (1 mg mL^{-1}) in a Teflon vessel under magnetic stirring. After 3 h, the solution was placed into a stainless autoclave at 140 °C for 4 h in an electric oven. After centrifugation, the precipitations were washed in distilled water several times. HMPBs were obtained after freeze drying.

Hemolysis Assay: Human blood was friendly provided by Shanghai Bloody Center. The red blood cells (RBCs) were obtained after removing the serum of human blood by centrifugation. Then we used PBS to wash the RBCs five times. Ninefold volume of PBS were added to dilute the cells; 0.3 mL of diluted RBCs suspension was mixed with (a) 1.2 mL of PBS as a negative control, (b) 1.2 mL of distilled water as a positive control, and (c) 1.2 mL of HMPBs PBS solution at concentrations ranging from 100 to 6400 ppm. The mixtures were then vortexed and left to stand for 2 h at room temperature. Then, the samples were centrifuged, and the absorbance of the supernatants at 541 nm was measured by UV–vis–NIR spectroscopy.

Drug Loading: HMPBs were first mixed with different concentrations of DOX in PBS. After stirring at room temperature in the dark for 24 h, DOX-loading HMPBs were collected by centrifugation. And the concentration of unbounded DOX was measured by UV–vis–NIR spectroscopy with absorption intensity at 485 nm. DOX drug loading capacity was measured using the following equation:

$$\text{Laoding capacity} = (\text{total DOX} - \text{unbounded DOX}) / \text{total HMPBs} \quad (4)$$

PFP Loading: After freezing drying, the DOX-loaded HMPBs (20 mg) were transferred into a 5 mL bottle with rubber plug. The air in the bottle was evacuated with a vacuum pump. Then 100 µL PFP was injected into the bottle. After ultrasonic oscillating in the ice-water for 2 min, DOX/PFP-loading HMPBs were dispersed in PBS for further use.

In Vitro Drug Release of DOX: DOX/PFP-loading HMPBs (2 mg) were packaged into a dialysis bag (MWCO = 8 kDa), and then immersed within 25 mL PBS solution at different pH (pH = 7.4 or 5.0) and temperature (37 or 42.5 °C) in a tube. At different time points, 3.0 mL solution was collected and measured by using UV–vis–NIR spectroscopy, and then back to the tube.

In Vitro Cytotoxicity of HMPBs: Human cervical carcinoma cells (Hela), murine breast cancer cells (4T1), and human pancreatic cancer cells (PANC1) were cultured in standard cell media cells seeded into 96-well plates were incubated in 5% CO_2 at 37 °C for 24 h. Then different concentrations of HMPBs were added into the 96-well plates and continued to be cultured for 24 h. Cell viability was determined using MTT reduction assay.

In Vivo Tissue Compatibility Assay: All of the animal procedures were conducted under the guidelines approved by Institutional Animal Care and Use Committee (IACUC) of the Chongqing Medical University. 18 female BALB/c nude mice aged six weeks (25–30 g) were randomly divided into three groups. Then all the mice in one group were intravenously injected with PBS buffer as the control group and the other two groups were intravenously injected with HMPBs in PBS (dose = 50 mg kg^{-1}, $n = 6$). The behaviors of mice were monitored every day. After 25 days and 50 days feeding, the mice were sacrificed, and the main tissues (heart, liver, spleen, lungs, and kidney) were obtained and stained with H&E for histopathological analysis by the optical microscope observation. Blood biochemistry data were obtained from mice after the intravenous injection of PBS buffer and HMPBs at various time points (0, 25, 50 days).

In Vitro Antitumor Activity: Hela, 4T1, and PANC1 were seeded into 96-well plates at a density of 10^4 cells per well and incubated in 5% CO_2 at 37 °C for 12 h. The culture medium was changed and cells were incubated with complete medium containing PBS (control), free DOX, HMPBs, HMPBs-PFP, HMPBs-PFP+DOX. The groups of free DOX and HMPBs-PFP+DOX have the same concentration of DOX ($C_{[DOX]}$ = 45 µg mL^{-1}). While the groups of HMPBs, HMPBs-PFP, and HMPBs-PFP+DOX have an equivalent HMPBs dosage ($C_{[HMPBs]}$ = 30 µg mL^{-1}). After 4 h of incubation, excess unbound materials were removed by rinsing three times with PBS. Fresh complete medium was then added to the wells. The cells of the groups, free DOX, HMPBs, and HMPBs+DOX, were exposed to 808 nm laser at power density of 1 W cm^{-2} for 5 min for photothermal and chemo-thermal therapy treatment. And then incubated again in 5% CO_2 at 37 °C for 24 h. Relative cell viabilities were determined by the standard MTT assay.

Pharmacokinetics and Biodistribution Studies: To develop the tumor model, Hela cells (3×10^6) suspended in 100 µL PBS solution were injected into the lateral thigh of each mouse. For pharmacokinetic experiments, female BALB/c nude mice bearing Hela tumors were injected intravenously with HMPBs in PBS ($n = 6$). 15 µL blood was collected at various time (0 min, 5 min, 10 min, 0.5 h, 1 h, 2 h, 4 h, and 24 h) after injection. The blood was dispersed into 1 mL physiological saline contained EDTA anticoagulation (10 mmol L^{-1}). The concentration of Fe^{3+} was measured by ICP-AES. The in vivo blood terminal half-life of HMPBs was calculated by a single-component pharmacokinetic model. Biodistribution of HMPBs in tumor and other organs was performed in Hela-tumor-bearing mice ($n = 6$). Mice were dissected with HMPBs in PBS (0.2 mL) at predesignated time points (2, 6, 12, 24, and 48 h). Dissected organs were weighed, homogenized, and treated with scintillation mixtures. The HMPBs distribution in different organs/tissues was calculated as the percentage of injected dose per gram of tissue.

In Vivo Infrared Thermal Imaging: To develop the tumor model, Hela cells (3×10^6) suspended in 100 µL PBS were injected into the lateral thigh of each mouse. The tumor-bearing female BALB/c nude mice were first anesthetized using trichloroacetaldehyde hydrate (10%) at a dosage of 40 mg kg^{-1} body weight while maintaining at normal body temperature. The mice were then injected with PBS (200 µL, $n = 3$) and DOX/PFP-loaded HMPBs in PBS through intravenous injection, respectively. The spatial temperature distribution of the nanoparticles were recorded by the thermalgraphy under the 808 nm laser irradiation.

In Vitro and In Vivo US and PA Imaging: All the US and PA imaging were obtained by Vevo LAZR photoacoustic imaging system (VisualSonics Company, Canada). Experiment parameter: Frequency: 21 MHz; PA gain: 40 dB: 2D gain: 18 dB; wavelength: 808 nm. US imaging of DOX/PFP-loaded HMPBs dispersed in PBS were obtain at 20 and 42 °C, respectively. In contrast, US imaging of PBS was achieved at 20 °C. The tumor-bearing female BALB/c nude mice were injected intravenously with DOX/PFP-loaded HMPBs (total dose = 200 µL, $C_{[DOX]}$ = 1.8 mg mL^{-1}, $C_{[HMPBs]}$ = 1.2 mg mL^{-1}, $n = 3$). The PA values of DOX/PFP-loaded HMPBs at various concentrations in vitro were investigated by Vevo LAZR photoacoustic imaging system. US and PA imaging were obtained before and 24 h after intravenous injection. Then, the tumors were exposed to 808 nm laser at the power density of 1 W cm^{-2} for 3 min. After irradiation, US and PA imaging were obtained immediately. And then, one tumor was dissected out for US and PA imaging.

In Vivo Synergistic Chemo-Thermal Therapy: The tumor-bearing female BALB/c nude mice were randomly allocated into five groups (control,

free DOX, HMPBs+NIR, HMPBs+DOX, HMPBs+DOX+NIR, $n = 7$ for each group). The mice in the treatment group were injected with free DOX, HMPBs-PFP, HMPBs-DOX/PFP, and HMPBs-DOX/PFP in PBS buffer (total dose = 200 μL, $C_{[DOX]} = 1.8$ mg mL^{-1}, $C_{[HMPBs]} = 1.2$ mg mL^{-1}, $n = 3$) by intravenous injection, respectively, while the tumor-bearing mice in the control group were only injected with PBS buffer (200 μL). Both HMPBs+DOX group and HMPBs+DOX+NIR group have an equivalent DOX dosage to the free DOX group ($C_{[DOX]} = 1.8$ mg mL^{-1}), and have an equivalent HMPBs dosage to the HMPBs+NIR group ($C_{[HMPBs]} = 1.2$ mg mL^{-1}). After 24 h, the tumors from group 3 and group 5 were irradiated with 808 nm laser (1 W cm^{-2}) for 3 min. One mouse was euthanized one day after the laser treatment from the two groups, respectively. The tumor dimensions were measured with a caliper, and the tumor volume was calculated according to the equation: Volume = (Tumor length) × (Tumor width)^2/2. After treatment for 26 days, most of the mice from the control group had to be euthanized prematurely, because their tumors had reached the ethical limit of 15 mm in diameter. Based on this, the relative tumor volume was recorded only until 26 days after treatment.

Statistical Analysis: Data were expressed as mean ± s.e.m. Differences between groups were assessed using the paired, two-sided Student t-test. $*P < 0.05$ was considered significant, and $**P < 0.01$ was considered highly significant.

Characterization: TEM/scanning transmission electron microscopy (STEM) images were acquired on a JEM-2100F electron on a field emission Magellan 400 microscope (FEI Company). Different imaging modes were employed to observe the microstructures of obtained nanoparticles, including second electron (SE), bright field (BF), dark field (DF), and high angle annular dark field (HAADF). Nitrogen adsorption–desorption isotherms at 77 K were measured on a Micrometitics Tristar 3000 system. DLS measurement was conducted on Zetasizer Nanosize (Nnao ZS90). UV–vis–NIR spectroscopy were recorded on a UV-3101PC shimadzu spectroscope. All the US and PA imaging were obtained by Vevo LAZR photoacoustic imaging system (VisualSonics company, Canada).

Supporting Information

Supporting Information is available from the Wiley Online Library or from the author.

Acknowledgements

This work was supported by the National Basic Research Program of China (973 Program, Grant No. 2011CB707905), China National Funds for Distinguished Young Scientists (51225202), National Natural Science Foundation of China (Grant Nos. 51072212 and 51132009), Shanghai outstanding academic leaders program (Grant No. 14XD1403800).

Received: November 11, 2014
Revised: January 22, 2015
Published online: February 27, 2015

[1] a) A. Gabizon, H. Shmeeda, Y. Barenholz, *Clin. Pharmacokinet.* **2003**, *42*, 419; b) G. Gregoriadis, *Trends Biotechnol.* **1995**, *13*, 527; c) T. Lian, R. J. Y. Ho, *J. Pharm. Sci.* **2001**, *90*, 667.
[2] Y. F. Zhu, J. L. Shi, W. H. Shen, X. P. Dong, J. W. Feng, M. L. Ruan, Y. S. Li, *Angew. Chem. Int. Ed.* **2005**, *44*, 5083.
[3] F. Q. Tang, L. L. Li, D. Chen, *Adv. Mater.* **2012**, *24*, 1504.
[4] a) A. M. Alkilany, L. B. Thompson, S. P. Boulos, P. N. Sisco, C. J. Murphy, *Adv. Drug Delivery Rev.* **2012**, *64*, 190; b) T. L. Doane, C. Burda, *Chem. Soc. Rev.* **2012**, *41*, 2885; c) G. von Maltzahn, J. H. Park, A. Agrawal, N. K. Bandaru, S. K. Das, M. J. Sailor, S. N. Bhatia, *Cancer Res.* **2009**, *69*, 3892; d) Z. H. Sheng, L. Song, J. X. Zheng, D. H. Hu, M. B. Zheng, G. H. Gao, P. Gong, P. F. Zhang, Y. F. Ma, L. T. Cai, *Biomaterials* **2013**, *34*, 5236; e) Z. H. Sheng, D. H. Hu, M. B. Zheng, P. F. Zhao, H. L. Liu, D. Y. Gao, P. Gong, G. H. Gao, P. F. Zhang, Y. F. Ma, L. T. Cai, *ACS Nano* **2014**, *8*, 12310.
[5] K. Yang, S. Zhang, G. Zhang, X. Sun, S. T. Lee, Z. Liu, *Nano Lett.* **2010**, *10*, 3318.
[6] a) T. S. Hauck, T. L. Jennings, T. Yatsenko, J. C. Kumaradas, W. C. W. Chan, *Adv. Mater.* **2008**, *20*, 3832; b) Z. Zhang, L. Wang, J. Wang, X. Jiang, X. Li, Z. Hu, Y. Ji, X. Wu, C. Chen, *Adv. Mater.* **2012**, *24*, 1418; c) X. Yang, X. Liu, Z. Liu, F. Pu, J. Ren, X. Qu, *Adv. Mater.* **2012**, *24*, 2890.
[7] T. Liu, C. Wang, X. Gu, H. Gong, L. Cheng, X. Shi, L. Feng, B. Sun, Z. Liu, *Adv. Mater.* **2014**, *26*, 3433.
[8] Z. J. Zhang, L. M. Wang, J. Wang, X. M. Jiang, X. H. Li, Z. J. Hu, Y. H. Ji, X. C. Wu, C. Y. Chen, *Adv. Mater.* **2012**, *24*, 1418.
[9] a) H. Y. Liu, D. Chen, L. L. Li, T. L. Liu, L. F. Tan, X. L. Wu, F. Q. Tang, *Angew. Chem. Int. Ed.* **2011**, *50*, 891; b) H. Y. Liu, T. L. Liu, X. L. Wu, L. L. Li, L. F. Tan, D. Chen, F. Q. Tang, *Adv. Mater.* **2012**, *24*, 755.
[10] M. Ma, H. Chen, Y. Chen, X. Wang, F. Chen, X. Cui, J. Shi, *Biomaterials* **2012**, *33*, 989.
[11] Z. Y. Xiao, C. W. Ji, J. J. Shi, E. M. Pridgen, J. Frieder, J. Wu, O. C. Farokhzad, *Angew. Chem. Int. Ed.* **2012**, *51*, 11853.
[12] W. Zhang, Z. Guo, D. Huang, Z. Liu, X. Guo, H. Zhong, *Biomaterials* **2011**, *32*, 8555.
[13] M. S. Yavuz, Y. Y. Cheng, J. Y. Chen, C. M. Cobley, Q. Zhang, M. Rycenga, J. W. Xie, C. Kim, K. H. Song, A. G. Schwartz, L. H. V. Wang, Y. N. Xia, *Nat. Mater.* **2009**, *8*, 935.
[14] L. R. Guo, D. D. Yan, D. F. Yang, Y. J. Li, X. D. Wang, O. Zalewski, B. F. Yan, W. Lu, *ACS Nano* **2014**, *8*, 5670.
[15] Y. Xia, W. Li, C. M. Cobley, J. Chen, X. Xia, Q. Zhang, M. Yang, E. C. Cho, P. K. Brown, *Acc. Chem. Res.* **2011**, *44*, 914.
[16] C. Li, *Nat. Mater.* **2014**, *13*, 110.
[17] a) J. W. Kim, E. I. Galanzha, E. V. Shashkov, H. M. Moon, V. P. Zharov, *Nat. Nanotechnol.* **2009**, *4*, 688; b) L. V. Wang, S. Hu, *Science* **2012**, *335*, 1458; c) K. Pu, A. J. Shuhendler, J. V. Jokerst, J. Mei, S. S. Gambhir, Z. Bao, J. Rao, *Nat. Nanotechnol.* **2014**, *9*, 233.
[18] a) H. Y. Lian, M. Hu, C. H. Liu, Y. Yamauchi, K. C. Wu, *Chem. Commun.* **2012**, *48*, 5151; b) L. Jing, X. Liang, Z. Deng, S. Feng, X. Li, M. Huang, C. Li, Z. Dai, *Biomaterials* **2014**, *35*, 5814; c) X. Liang, Z. Deng, L. Jing, X. Li, Z. Dai, C. Li, M. Huang, *Chem. Commun.* **2013**, *49*, 11029.
[19] G. L. Fu, W. Liu, S. S. Feng, X. L. Yue, *Chem. Commun.* **2012**, *48*, 11567.
[20] a) Y. Chen, H. Chen, D. Zeng, Y. Tian, F. Chen, J. Feng, J. Shi, *ACS Nano* **2010**, *4*, 6001; b) W. Zhao, H. Chen, Y. Li, L. Li, M. Lang, J. Shi, *Adv. Funct. Mater.* **2008**, *18*, 2780.
[21] J. Zeng, D. Goldfeld, Y. Xia, *Angew. Chem. Int. Ed.* **2013**, *52*, 4169.
[22] N. W. Kam, M. O'Connell, J. A. Wisdom, H. Dai, *Proc. Natl. Acad. Sci. U.S.A.* **2005**, *102*, 11600.
[23] C. M. Hessel, V. P. Pattani, M. Rasch, M. G. Panthani, B. Koo, J. W. Tunnell, B. A. Korgel, *Nano Lett.* **2011**, *11*, 2560.
[24] Q. Tian, F. Jiang, R. Zou, Q. Liu, Z. Chen, M. Zhu, S. Yang, J. Wang, J. Wang, J. Hu, *ACS Nano* **2011**, *5*, 9761.
[25] P. Huang, J. Lin, W. Li, P. Rong, Z. Wang, S. Wang, X. Wang, X. Sun, M. Aronova, G. Niu, R. D. Leapman, Z. Nie, X. Chen, *Angew. Chem. Int. Ed.* **2013**, *52*, 13958.
[26] a) G. M. Hahn, J. Braun, I. Harkedar, *Proc. Natl. Acad. Sci. U.S.A.* **1975**, *72*, 937; b) H. Park, J. Yang, J. Lee, S. Haam, I.-H. Choi, K.-H. Yoo, *ACS Nano* **2009**, *3*, 2919.
[27] H. Xing, X. Zheng, Q. Ren, W. Bu, W. Ge, Q. Xiao, S. Zhang, C. Wei, H. Qu, Z. Wang, Y. Hua, L. Zhou, W. Peng, K. Zhao, J. Shi, *Sci. Rep.* **2013**, *3*, 1751.
[28] M. Hu, S. Furukawa, R. Ohtani, H. Sukegawa, Y. Nemoto, J. Reboul, S. Kitagawa, Y. Yamauchi, *Angew. Chem. Int. Ed.* **2012**, *51*, 984.